



# The microstructure and mechanical behavior of Mg/Ti multilayers as a function of individual layer thickness

Y.Y. Lu<sup>a</sup>, R. Kotoka<sup>b</sup>, J.P. Ligda<sup>c</sup>, B.B. Cao<sup>a</sup>, S.N. Yarmolenko<sup>b</sup>, B.E. Schuster<sup>c</sup>,  
Q. Wei<sup>a,\*</sup>

<sup>a</sup> Department of Mechanical Engineering, The University of North Carolina at Charlotte, Charlotte, NC 28223-0001, USA

<sup>b</sup> Department of Mechanical Engineering, NC A&T State University, Greensboro, NC 27411, USA

<sup>c</sup> WMRD, US Army Research Laboratory, Aberdeen Proving Ground, Aberdeen, MD 21005, USA

Received 19 June 2013; received in revised form 13 October 2013; accepted 15 October 2013

Available online 14 November 2013

## Abstract

We have used magnetron sputtering to deposit magnesium and titanium layers alternately onto a single-crystal silicon substrate with equal individual layer thickness ( $h$ , from 2.5 to 200 nm) to form multilayers. We have investigated the mechanical behavior of the multilayers and its dependence on  $h$ . Transmission electron microscopy and X-ray diffraction analyses suggest that the multilayers exhibit strong texture with respect to Mg (0002) and Ti (0002) with an epitaxial growth pattern. Two primary orientation relationships between Ti and Mg have been identified, depending on  $h$ . Instrumented nanoindentation and microcompression have been used to examine the hardness/strength and the strain rate sensitivity of the multilayers. Based on nanoindentation, we have found that the strength of these multilayers generally increases as  $h$  is decreased. The microcompression measured strength is remarkably higher than that derived from indentation. The Hall–Petch law can be used to interpret the increase in strength at relatively large  $h$  ( $>50$  nm), while the confined layer slip model provides a better explanation for the relationship between strength and  $h$  at smaller  $h$ . We have also attempted to present an in-depth discussion about the applicability of relevant strengthening mechanisms on these hexagonal close-packed/hexagonal close-packed multilayers.

© 2013 Acta Materialia Inc. Published by Elsevier Ltd. All rights reserved.

**Keywords:** Multilayered nanofilm; Magnesium; Titanium; Microstructure; Strength

## 1. Introduction

Metallic multilayers with individual layer thickness ( $h$ ) ranging from the submicron scale to the nanometer scale are drawing ever-increasing attention from the materials science community at large. One of the primary reasons for this phenomenon lies in the motivation to exploit the strength of metallic materials. The synthesis of strong solids for structural as well as functional applications has been one of the ultimate goals of materials engineers [1,2]. Recent efforts have shown that metallic multilayers composed of constituent metals, either with the same lattice

type or with heterogeneous lattice types, can exhibit impressive mechanical properties, especially high strength [3–6]. Furthermore, for a binary system, the two metals may be intermiscible (and even isomorphous, such as copper and nickel) or immiscible at equilibrium. Metallic multilayers between crystalline metals and metallic glasses have also been produced and investigated, with some novel mechanisms identified [7]. Therefore, metallic multilayers have opened a new and exciting arena to materials science and engineering and mechanical engineering. Potential applications include X-ray optics, hydrogen storage, wear and thermal resistance coating, and microelectromechanical systems (MEMS) [8–11].

The combination of two or more components with fine-tuned lamellar arrangement can now be fulfilled and

\* Corresponding author. Tel.: +1 704 687 8213; fax: +1 704 687 8345.  
E-mail address: [qwei@uncc.edu](mailto:qwei@uncc.edu) (Q. Wei).

accurately controlled by various physical deposition techniques. So far, a number of studies have been reported about the microstructure and mechanical behavior of multilayered composites consisting of face-centered cubic (fcc) and body-centered cubic (bcc) structures, including Cu/Nb (fcc/bcc), Cu/Ni (fcc/fcc), Cu/Cr (fcc/bcc), Cu/Ag (fcc/fcc), Al/Nb (fcc/bcc), Cu/V (fcc/bcc), Ag/Ni (fcc/fcc) and Cu/Au (fcc/fcc) [12–22]. Their dependence of strength on the individual layer thickness  $h$  has been investigated through both experiments and atomistic simulations. Three deformation mechanisms have been identified operating within various regimes of  $h$  [23–27]. When  $h$  is large enough, usually about a few hundreds of nanometers, the Hall–Petch law, which is attributed to dislocation pile-ups at layer interfaces, plays a dominant role. The yield strength increases with decreasing  $h$ , following  $\sigma \sim h^{-0.5}$ . As  $h$  decreases to several tens of nanometers or even less, there are insufficient dislocations for the pile-up model to operate because now the spacing between adjacent layers is too small [28]. At this level of  $h$ , bowing out of single dislocations and their glide within the layers are proposed to account for the slower increase rate of strength with decreasing  $h$ . In other words, in this regime, the conventional Hall–Petch law levels off. This mechanism has been dubbed the confined layer slip (CLS) model and has been widely accepted in the community, even though it has been modified by various investigators so as to remedy the deficiency of the Hall–Petch law in explanation for the strength evolution in multilayered metallic composites [29]. The subsequent transmission of dislocations across the layer interface leads to a peak strength associated with the commonly observed strength plateau when  $h$  is below a critical value. In this case, the interface barrier strength (IBS) becomes a critical parameter, and calculations of IBS generally involve finding the coherency stress related to the mismatch strain from the difference in lattice parameters and the image stress due to the discrepancy of shear modulus between the constituents [5,30,31].

A quick literature survey shows that most of the efforts on the syntheses and characterizations of multilayered metallic composites focus on systems composed of cubic components such as fcc/bcc or fcc/fcc types [6,12–21,23,25–27,30,32–36]. Recently cubic/hexagonal close packed (hcp) systems, such as Cu/Zr (fcc/hcp) and Mg/Nb (hcp/bcc) have started to attract attention from investigators [37,38]. However, considering the technological and scientific importance of many metals with hcp lattice structures, such as magnesium, titanium and beryllium, much greater efforts are needed to exploit the unique characteristics of such metals, particularly in the context of multilayer systems. First of all, unlike cubic metals, which are usually ductile due to the profuse slip systems available, hcp metals have many fewer slip systems. For example, in single-crystal and polycrystalline Mg, the dominant slip mechanism is the basal slip ( $\{0001\}/\langle 11\bar{2}0 \rangle$ ) [39], even though other slip systems such as prismatic ( $\{10\bar{1}0\}/\langle 11\bar{2}0 \rangle$ ) and pyramidal ( $\{10\bar{1}1\}/\langle 11\bar{2}0 \rangle$ ) slip

systems have been observed under some special loading conditions and with special microstructures and chemical compositions [40,41]. As for  $\alpha$ -Ti, the dominant slip system is prismatic slip under ordinary conditions ( $\{10\bar{1}0\}/\langle 11\bar{2}0 \rangle$ ) [42,43]. These metals have become increasingly important due to their light weight or even ultra-light weight (the mass density of Mg is only  $1.74 \text{ g cm}^{-3}$ , compared to  $7.9 \text{ g cm}^{-3}$  for steels) and impressive mechanical stiffness, which together render extraordinarily high specific strength.

To the best of our knowledge, there has been no work reporting the synthesis, microstructure and mechanical properties of metallic multilayers between hcp metals. Pd-capped Mg/Ti multilayers were deposited by DC and radiofrequency magnetron sputtering, but the focus was on the capacity and kinetics of hydrogen storage of such multilayers and the maximum thickness of the coating was only 60 nm [44]. It might be argued that some of the multilayered composites reported in the literature consist of one hcp component [37,38].

However, multilayers composed of monolithic and stable hcp crystals have not been reported yet in the context of microstructure–mechanical properties relationships.

In this study, two commonly used hcp metals, magnesium and titanium, were selected to prepare multilayers with various  $h$  (2.5–200 nm). We have chosen Mg and Ti firstly because both are hcp metals at room temperature. These two hcp metals are also mutually immiscible, and thus may lead to high thermal and compositional stability of the multilayers. Ti and Mg have a moderate lattice mismatch. The microstructure and mechanical properties of the Mg/Ti multilayers were carefully examined to obtain a comprehensive understanding of the microstructural evolution and strengthening mechanisms as a function of  $h$ .

## 2. Experimental details

In what follows, we provide a detailed description about the experimental procedures of this work, including materials processing, microstructural characterization and mechanical property evaluation using instrumented nano-indentation as well as microcompression.

### 2.1. Preparation of Mg/Ti multilayers

In this work, we follow the efforts in the literature on metallic multilayers where most multilayers have been synthesized via physical vapor deposition such as electron beam evaporation and magnetron sputtering. Although other techniques have also been used to produce nanometer metallic multilayers, such as accumulative roll bonding (ARB) [33,45], we chose magnetron sputtering due to its ease of operation and fast turn-around. In the present work, high-purity Mg and Ti were deposited alternately onto a single-crystal (100) silicon substrate with nearly identical  $h$  ranging from 2.5 to 200 nm using an ATC 1800-F system (AJA International Inc.). The

deposition chamber is capable of housing four targets with computer-controlled shutters for all the targets. The deposition rates of Ti and Mg under  $\sim 1.0$  mtorr Ar pressure were 0.136 and 0.417 nm s $^{-1}$ , respectively. The individual layer thickness was monitored by X-ray reflectivity (XRR) measurement. Through the control of bilayer periodicity, the total multilayer thickness of each specimen was kept at  $\sim 1.0$   $\mu\text{m}$  when  $h < 100$  nm. For the sample with thicker layers (200 nm), the total thickness was  $\sim 5.0$   $\mu\text{m}$ . The silicon substrate was cleaned with plasma within the chamber for 10 min prior to multilayer deposition to remove surface contamination and the native oxide layer. In all the samples, a 2 nm thick Ti layer was first deposited on the silicon substrate since Si and Ti have relatively strong chemical bonding. Because Mg is very reactive, the top layer of all the multilayers is Ti to avoid sample degradation with time after retrieval from the chamber. For all the depositions, the substrate temperature was kept at room temperature.

## 2.2. Microstructural characterization

X-ray related experiments are not only useful in analyzing the possible phases in the multilayers, but are also rapid and non-destructive ways to measure  $h$  [46,47]. In this work, we used a Bruker AXS D8 Discover X-ray diffractometer (using Cu K $\alpha$  radiation) to perform XRR and X-ray diffraction (XRD) analyses. We used both low-angle XRR ( $2\theta < 15^\circ$ ) and high-angle XRD ( $2\theta > 15^\circ$ ) to examine the bilayer period  $\Lambda$  ( $\Lambda = h_{\text{Mg}} + h_{\text{Ti}}$ ) of the Mg/Ti multilayers. The XRR and XRD results are compared against each other to verify the appropriate modulation. XRR can provide the thickness information through the reflection of the incident X-rays off the interfaces between the layers. Several periodic peaks could be detected at small angles, such as those displayed in Fig. 1b.

High-angle XRD of multilayers usually shows equally spaced satellite peaks surrounding the ordinary and primary Bragg peaks because of the similar out-of-plane lattice spacing, as shown in Fig. 1c. Analysis of these satellite peaks also provides information of  $h$ .

The cross-sectional microstructures of the Mg/Ti multilayers were examined by transmission electron microscopy (TEM) and high resolution transmission electron microscopy (HRTEM) on the JEOL 2100 microscope operated at 200 kV. All the TEM samples were made by the focused ion beam (FIB) technique on an FEI Nova 600i dual beam FIB system (US Army Research Laboratory).

## 2.3. Evaluation of mechanical behavior

Nanoindentation tests were carried out on an Agilent NanoIndenter G200 with a Berkovich diamond tip. The commonly used continuous stiffness method was applied to measure the hardness  $H$  and Young's modulus  $E$  of

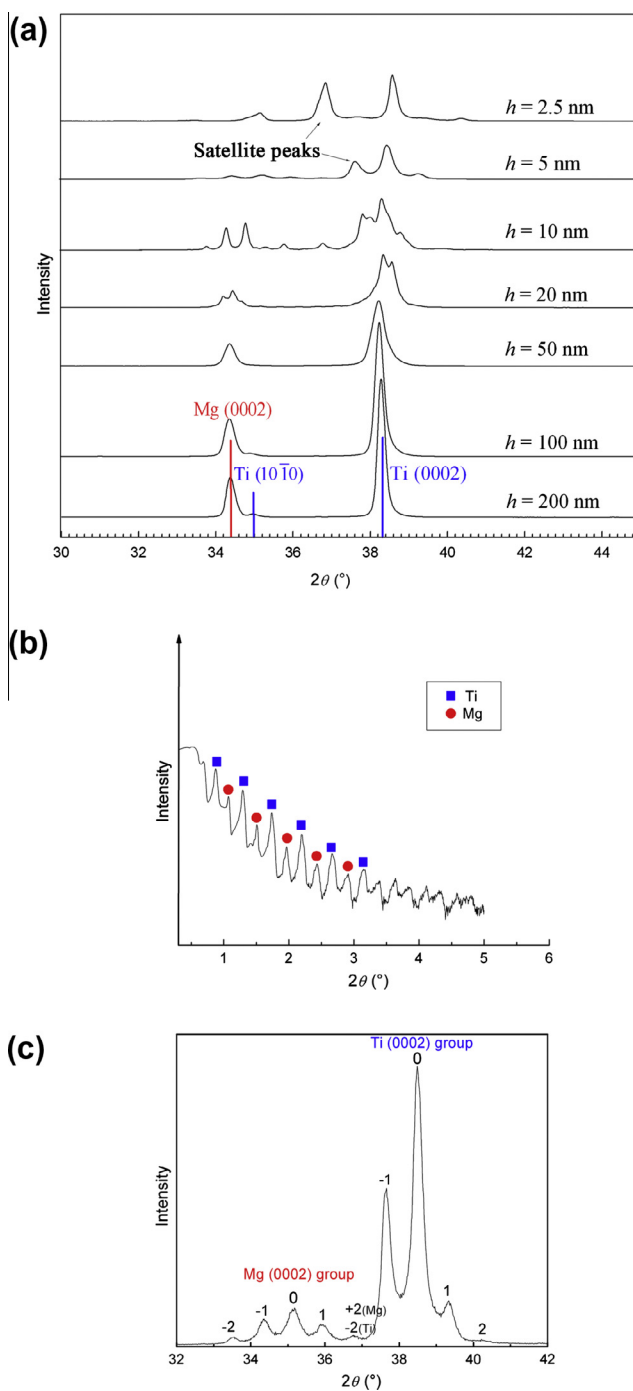


Fig. 1. (a) XRD results of Mg/Ti multilayered nanofilms with various individual layer thicknesses  $h$  (from  $h = 2.5$  nm to  $h = 200$  nm). The primary diffraction peaks correspond to Mg (0002) and Ti (0002) (the basal planes). For large individual layer thickness such as 100 and 200 nm, Ti (10 $\bar{1}$ 0) reflections become visible. It is also observed that the peak breadth becomes larger with decreased  $h$ . Satellite peaks start to emerge around the primary peaks at small  $h$ , too, indicating the modulated structure with small wavelength of high spatial frequency. (b) XRR of the nanofilm with  $h = 50$  nm, showing the peaks associated with the Ti and Mg layers. The information contained in such XRR results is used to derive the periodicity of the layers. (c) Magnified XRD of the nanofilm with  $h = 5$  nm, showing the various orders of satellite peaks that will be used to calculate the periodicity of the layers.

the multilayers at a constant strain rate of  $0.05 \text{ s}^{-1}$  (without specific indication, hardness or flow strength mentioned in the following were measured at this strain rate, and the issue of strain rate sensitivity (SRS) will be addressed separately). The hardness value reached a plateau and became stable when the indentation depth exceeded 50 nm in our tests before a significant substrate effect kicks in. Following the rule proposed by Buckle [48], the nanoindentation data were collected within a maximum indenting depth of  $\sim 10\text{--}15\%$  of the whole thickness for each multilayer specimen to reduce the substrate effects.

Since SRS is an important fingerprint for the plastic deformation mechanisms of materials [49,50], we also evaluated the SRS of the multilayers using nanoindentation. In this case, the hardness of the specimens was measured at different strain rates defined by

$$\dot{\epsilon} = \frac{\dot{P}}{2P} \quad (1)$$

where  $P$  is the load and  $\dot{P} = dP/dt$  is the loading rate. In this study, the nanoindentation tests were carried out at strain rates of 0.005, 0.01, 0.05 and  $0.1 \text{ s}^{-1}$  on the Mg/Ti multilayers. The SRS,  $m$ , in terms of hardness, is defined by

$$m = \frac{\partial \log H}{\partial \log \dot{\epsilon}} \quad (2)$$

To keep the consistency with the flow strength (obtained by dividing the hardness by a factor of 2.7 based on the Tabor relationship [51]), the activation volume associated with plastic deformation is then calculated as

$$V^* = \frac{2.7 \times \sqrt{3}kT}{H \cdot m} \quad (3)$$

In Eq. (3),  $k$  is the Boltzmann constant and  $T$  the absolute temperature (in K). Recently there have been efforts on this subject from different groups [29,32] in the context of metallic multilayer systems.

Since its advent, microcompression has become a powerful technique to probe the stress–strain behavior of small volumes [52]. It has also been applied to metallic multilayers for direct measurement of the mechanical behavior of the samples [32,34,53]. In this work, we have fabricated micropillars of the Mg/Ti multilayers using FIB. An approximate aspect ratio of pillar height:diameter of 2:1 was followed according to the recommendation of Zhang et al. [54]. The microcompression experiments were performed on a Nanoindenter XP I with a flat diamond punch pressing against the pillar top. Post-loading examinations of the pillars were performed within the dual beam system (FEI Nova 600i). Fig. 2 displays an example of micropillars fabricated by FIB of the Mg/Ti multilayer specimens.

### 3. Experimental results

In what follows, we will present the experimental results of this work, including microstructures of the

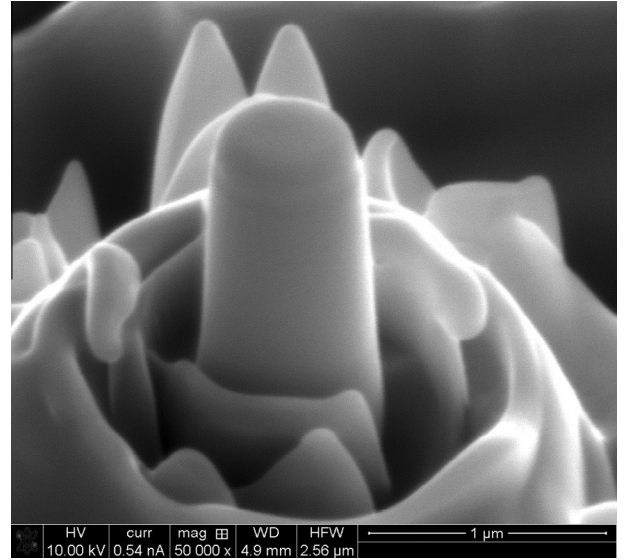


Fig. 2. An example of the micropillars extracted from an Mg/Ti multilayered specimen ( $h = 2.5 \text{ nm}$ ) by focused ion beam (FIB) for the microcompression experiment. The pillar is slightly tapered, which is an unavoidable consequence for such small pillars fabricated by FIB.

Mg/Ti multilayers based on XRD, XRR and TEM. This is followed by mechanical testing results based on nanoindentation and microcompression. Finally, some post-loading microstructure results will be provided on the pillar samples.

#### 3.1. Microstructures of the Mg/Ti multilayers

Fig. 1a provides the XRD results of various Mg/Ti multilayers with different  $h$ . It is clearly seen that Mg and Ti are both highly textured along Mg (0002) and Ti (0002). Very weak intensity is observed from Ti ( $10\bar{1}0$ ) reflections for  $h = 100 \text{ nm}$  and  $200 \text{ nm}$ , respectively. We will see later in this paper that such texture imparts strong effects on the mechanical behavior of the multilayers, particularly pertaining to the compression behavior. The ( $10\bar{1}0$ ) peak disappears for smaller  $h$ . This suggests that when  $h$  is smaller, preferentiality in orientation becomes stronger. Our TEM results to be presented later on will show that epitaxial growth between the Ti layer and the Mg layer has occurred for small  $h$ . This is indirectly suggested by the prevalence of Mg (0002)/Ti (0002) peaks, and disappearance of all other reflections when  $h \leq 50 \text{ nm}$  (Fig. 1a). In particular, both Bragg peaks of Mg (0002) and Ti (0002) shift to larger angles gradually as  $h$  is reduced. Satellite peaks start to emerge symmetrically about the Bragg peaks of Mg (0002)/Ti (0002) reflections in the XRD spectra when  $h \leq 20 \text{ nm}$ . Higher-order satellite peaks become visible when the XRD pattern is amplified about the major Bragg peaks, as shown in Fig. 1c for  $h = 5 \text{ nm}$ .

The bilayer period  $\Lambda$ , which is the sum of the individual thickness of the Ti and Mg single layers ( $\Lambda = h_{\text{Ti}} + h_{\text{Mg}}$ ), is determined from the XRD data following standard

Table 1  
The values of bilayer period  $\Lambda$  measured by low angle XRR and high angle XRD for the Mg/Ti multilayers.

Designed bilayer period $\Lambda$ ( $\Lambda = h_{\text{Mg}} + h_{\text{Ti}}$ ) (nm)	$\Lambda$ measured from XRR (nm)		$\Lambda$ measured from XRD (nm)	
	Average	Error	Average	Error
10 (5 + 5)	11.27	0.52	11.22	0.05
20 (10 + 10)	19.31	0.79	18.27	0.05
40 (20 + 20)	37.7	1.8	37.11	0.07
100 (50 + 50)	93.6	9.1	–	–
200 (100 + 100)	197	28	–	–

procedure. The results for the various specimens are summarized in Table 1. The very small discrepancy between XRD results and the designed bilayer periodicity indicates that the XRD measurements of periodicity in the multilayers based on the position of satellite peaks are quite reliable. It also suggests that relatively accurate modulation and control of Mg and Ti laminates have been achieved in our study.

Since these two hcp metals were deposited alternately to build up the whole multilayer specimen, their corresponding peaks on the XRR patterns also appear in an alternate manner. An example is provided in Fig. 1b, which is the XRR results of the 50 nm Mg/50 nm Ti multilayer in the small scanning angle regime. The peaks of Mg and Ti are equally spaced, and their positions have a nearly proportional relationship with the order of reflection. Based on the XRR results, we can also derive the average bilayer thicknesses for the specimens, with the results given in Table 1. The data in Table 1 show that the results from XRR are in very good agreement with those from XRD. As mentioned previously, both Mg and Ti grow preferentially in the direction perpendicular to the basal plane (or in the  $c$ -axis direction). This parallel growing behavior provides indirect evidence for epitaxial growth between Ti and Mg in the Mg/Ti multilayers, particularly for small  $h$ . Epitaxial growth between nanolayers has also been observed in other deposited films [55,56].

Fig. 3a is the bright-field TEM image showing the cross-sectional microstructure of the Mg/Ti multilayer with  $h = 10$  nm. Despite the uniform lamellar morphology across the whole cross-sectional view, two major orientation relationships (ORs) can be identified between Mg and Ti, and these are labeled OR.1 and OR.2, respectively, in the image. Selected area diffraction (SAD) patterns corresponding to the two boxed regions, designated as OR.1 and OR.2, in Fig. 3a are displayed in Fig. 3b and c, respectively. OR.1 refers to the orientation relationship of Mg  $\{0002\}$ //Ti  $\{0002\}$  and Mg  $\langle 01\bar{1}0 \rangle$ //Ti  $\langle 01\bar{1}0 \rangle$ , confirming the epitaxial growth between the two hcp components.

Considering the relatively large lattice mismatch between hcp Mg and Ti ( $a_{\text{hcp-Mg}} = 0.3209$  nm;  $a_{\text{hcp-Ti}} = 0.2951$  nm, and the mismatch is then 8.6% on the basal plane), the epitaxial growth appears remarkable.

In the second orientation relationship, OR.2, the Mg lattice maintains the same growing direction as that in OR.1, but the Ti lattice changes to develop along the axis

perpendicular to the prismatic plane  $(01\bar{1}0)$ , whose reflections was also detected by XRD. Therefore, this leads to another orientation relationship (OR.2), Mg  $\{0002\}$ //Ti  $\{01\bar{1}0\}$  and Mg  $\langle 2\bar{1}\bar{1}0 \rangle$ //Ti  $\langle 0001 \rangle$ .

However, OR.2 could hardly be detected by examining the whole cross-sectional microstructure of the specimen of  $h = 2.5$  nm. Fig. 4a shows a bright-field TEM image of the multilayer structure in this specimen. Besides OR.1, there is yet another orientation relationship Mg  $\{0002\}$ //Ti  $\{0002\}$  and Mg  $\langle 2\bar{1}\bar{1}0 \rangle$ //Ti  $\langle 2\bar{1}\bar{1}0 \rangle$  identified for this specimen, as shown in Fig. 4b. This relationship also reflects the epitaxial growth between Mg and Ti while the in-plane rotation of crystals contributes to its minor difference from OR.1. From the SAD pattern in Fig. 4b, the spots are seen to split into several strings due to the extremely fine lamellar structure, which is called streaking [57]. For this specimen Mg and Ti exclusively follow the orientation relationship of Mg  $\{0002\}$ //Ti  $\{0002\}$ . This is further confirmed by direct observations of the atomic arrangement of each layer via high-resolution TEM, with a representative image provided in Fig. 4c, where the orientation relationship has been marked out. The average spacing between two adjacent Mg atomic layers along the direction normal to the Mg/Ti interface is measured to be 2.58 Å, which is very close to half of the lattice parameter in the  $c$ -axis of hcp Mg, i.e.  $c_{\text{Mg}} = 5.21$  Å. The Ti layers exhibit similar characters. Along the  $[0002]$  direction (Fig. 4c), all the Mg and Ti atoms are stacking with a nearly perfect ABAB... sequence. At the interfaces, when the last “A” layer of Mg is finished, the subsequently deposited Ti atoms prefer to occupy atomic positions identical to the “B” layer. Nevertheless, the first two atomic layers of Ti are likely to shear themselves to a certain extent from direct observations, similar to a stacking fault in a monolithic hcp crystal. This small distortion is reasonable since the lattice at the vicinity of the Mg/Ti interface is strained due to the lattice mismatch between Mg and Ti. At relatively large  $h$ , epitaxial growth by means of domain-matching epitaxy [58,59] may still be possible, accompanied by the formation of misfit dislocations during the deposition process.

In summary, we have observed that depending on  $h$ , two major types of orientation relationship have been identified in the Mg/Ti multilayer specimens. For very small  $h$ , epitaxial deposition between Ti and Mg matching the basal plane has been the prevalent growth mode in spite of the

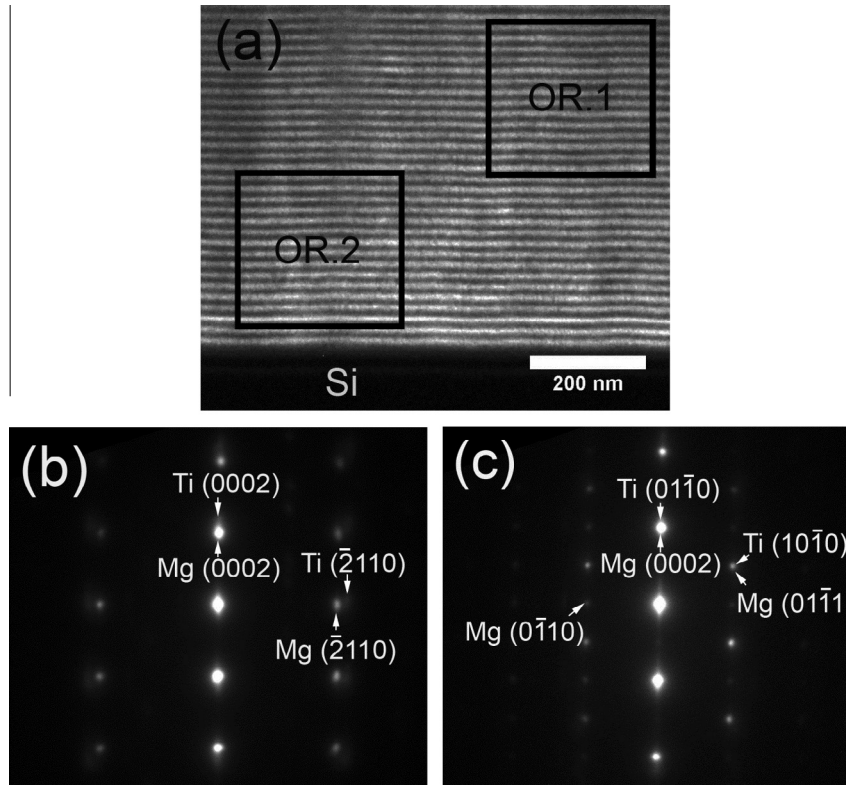


Fig. 3. (a) The bright-field TEM micrograph of the cross-sectional area of the Mg/Ti multilayered nanofilm with an individual layer thickness of 10 nm. The two boxed regions in this image correspond to the diffraction patterns of (b) and (c), respectively. The orientation relationship between Ti and Mg corresponding to (b) is OR.1: Mg  $\{0002\}$ //Ti  $\{0002\}$  and Mg  $\langle 01\bar{1}0 \rangle$ //Ti  $\langle 01\bar{1}0 \rangle$ . The orientation relationship corresponding to (c) is OR.2: Mg  $\{0002\}$ //Ti  $\{01\bar{1}0\}$  and Mg  $\langle 2\bar{1}\bar{1}0 \rangle$ //Ti  $\langle 0001 \rangle$ . Note that in OR.1 the basal planes of both the Mg and the Ti phases are parallel to the specimen surface or the Ti/Mg interfaces. In OR.2, the prism plane of the Ti phase is parallel to the Ti/Mg interfaces but the basal plane of Mg is still parallel to the Ti/Mg interfaces.

relatively large lattice mismatch between hcp Mg and Ti, resulting in an orientation relationship of Mg  $\{0002\}$ //Ti  $\{0002\}$  and Mg  $\langle 01\bar{1}0 \rangle$ //Ti  $\langle 01\bar{1}0 \rangle$  (or Mg  $\langle 2\bar{1}\bar{1}0 \rangle$ //Ti  $\langle 2\bar{1}\bar{1}0 \rangle$  with in-plane rotation of crystals). When  $h$  is increased, another orientation relationship, Mg  $\{0002\}$ //Ti  $\{01\bar{1}0\}$  and Mg  $\langle 2\bar{1}\bar{1}0 \rangle$ //Ti  $\langle 0001 \rangle$ , starts to emerge, presumably to accommodate the lattice mismatch and internal stress.

### 3.2. Mechanical behavior of the Mg/Ti multilayers

From nanoindentation experiments following the methods of Oliver and Pharr [60], we obtained the Young's modulus  $E$  and average hardness  $H$  of the as-deposited Mg/Ti multilayers. We have found that regardless of the various  $h$  values, the measured Young's modulus values are consistently in the range of  $78 \pm 6$  GPa. Considering that the room temperature Young's moduli of pure Mg and  $\alpha$ -Ti are 44 and 116 GPa, respectively, this result suggests that the "rule of mixture" applies to the Young's modulus of the Mg/Ti multilayers. Namely, the Young's modulus of the multilayer specimen is the weighted mean of the Young's moduli of the constituent components.

The hardness of the Mg/Ti multilayers exhibits an obvious increasing trend with  $h$ . Fig. 5 displays the

nanoindentation results of the various Mg/Ti multilayers. The maximum hardness with a magnitude of  $\sim 4.2$  GPa is obtained in the Mg/Ti multilayer of  $h \sim 2.5$  nm. To provide a more straightforward illustration of the deformation mechanisms in these hcp/hcp multilayers that we will revisit in the next section, we have plotted the flow strength  $\sigma$  (hardness  $H$  divided by a factor of 2.7) as a function of the inverse square root of  $h$  ( $h^{-0.5}$ ) in Fig. 5. This plot is reminiscent of strength– $h$  plots of many other multilayer systems in the literature [14,22,23]. In other words, when  $h$  is large, there is a nearly linear effect of  $h^{-0.5}$  on strength, following the classical Hall–Petch relation. However, when  $h$  is further reduced, its effect on strength levels off, until a decrease in strength is observed, which is popularly called the inverse Hall–Petch effect, as observed in bulk nanocrystalline metals [61]. However, a clear trend of the inverse Hall–Petch effect cannot be securely established for the Mg/Ti multilayer system since the maximum hardness is obtained at the smallest  $h$  ( $h = 2.5$  nm). The Hall–Petch effect has often been well explained by dislocation pile-ups within individual layers in the community of metallic multilayers [6,23]. In bulk polycrystalline metals, however, other equally valid models have been proposed to account for the Hall–Petch relation, including grain boundaries as dislocation sources and sinks [62],

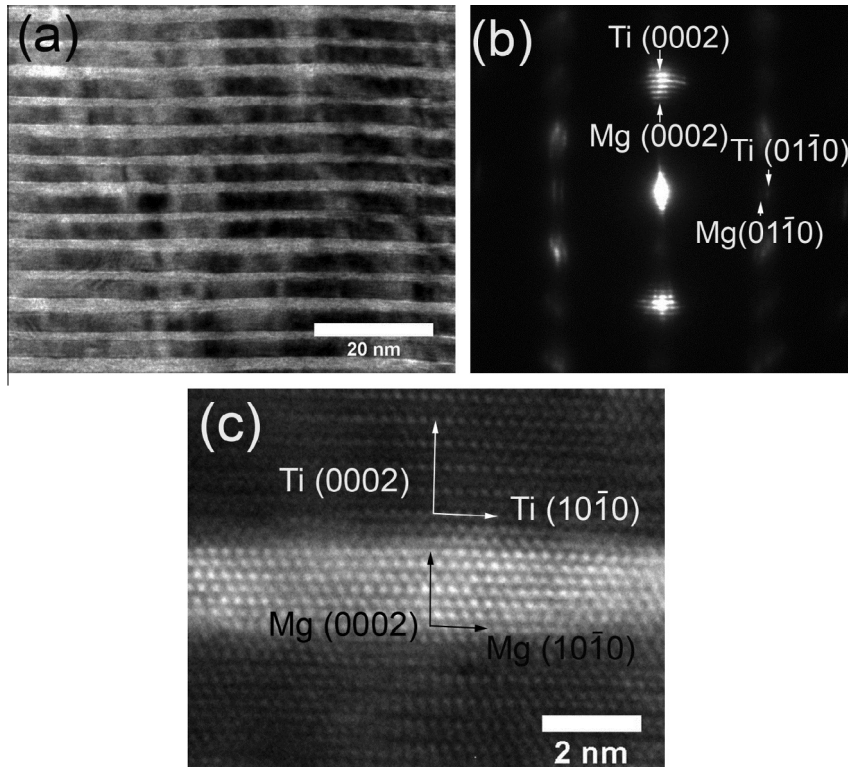


Fig. 4. (a) The bright-field TEM micrograph of the cross-sectional area of the Mg/Ti multilayered nanofilm with an individual layer thickness of 2.5 nm. (b) Beside OR.1, another orientation relationship, Mg {0002}//Ti {0002} and Mg  $\langle 2\bar{1}\bar{1}0 \rangle$ //Ti  $\langle 2\bar{1}\bar{1}0 \rangle$ , has been identified from the electron diffraction patterns of this specimen, also indicating the epitaxial growth between Mg and Ti. The only difference between it and OR.1 is the in-plane rotation of both Mg and Ti crystals. The streaking in the diffraction pattern is due to the extremely small individual layer thickness. (c) High-resolution TEM image of the Mg and Ti layers of this specimen, showing epitaxial growth between Mg and Ti.

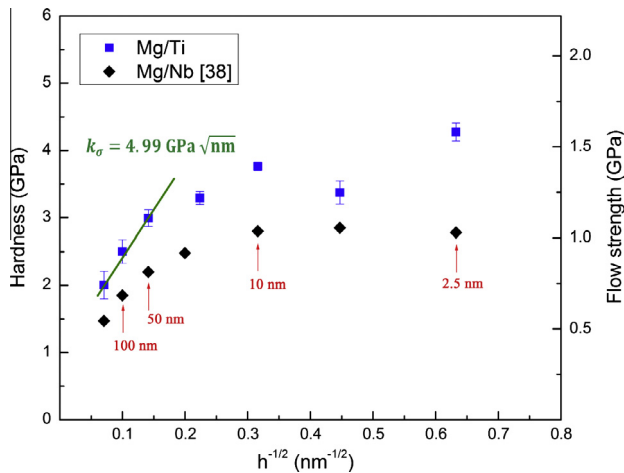


Fig. 5. The plot of nanoindentation hardness  $H$  and flow strength  $\sigma$  as a function of  $h^{-0.5}$  for the Mg/Ti multilayered specimens. For comparison, the results from an Mg/Nb multilayered system are also plotted. The results of the Mg/Nb system are from Ref. [38]. The flow strength is derived by dividing the nanoindentation hardness by a factor of 2.7. It can be observed that when the individual layer thickness  $h$  is large, the strength of the multilayer specimens follows the Hall–Petch relation. The strength levels off at a relatively small individual layer thickness, and a dip is observed at  $h = 5$  nm. However, the maximum strength is obtained at the smallest individual layer thickness of this work ( $h = 2.5$  nm).

geometrically necessary dislocation for plastic compatibility at the grain boundaries [63] and avalanche behavior

of dislocations [64], and so on. For comparison, in Fig. 5, we have also plotted the hardness of Mg/Nb multilayers. The data is extracted from Ref. [38] (the work of Ham and Zhang). We see that the hardness of this more heterogeneous system has been surpassed by the hcp/hcp system of Mg/Ti.

In Fig. 5, a straight line reflecting the Hall–Petch slope  $k_\sigma$  is sketched out in green to fit the linear relationship of  $\sigma \sim h^{-0.5}$  for relatively large  $h$ . The Hall–Petch slope  $k_\sigma$  is derived to be  $4.99 \text{ GPa nm}^{1/2}$ . As we have pointed out, with further reduction in  $h$ , the strength of the multilayers continues to increase but the Hall–Petch slope has been decreased compared to the value of  $k_\sigma$  for large  $h$ . We have also observed a dip in the strength vs.  $h^{-0.5}$  plot in the small  $h$  regime that occurs at  $h = 5$  nm. Afterwards, the strength increase resumes and the maximum flow strength,  $\sim 1.56$  GPa, is reached in the film with the smallest  $h$  ( $\sim 2.5$  nm). The commonly observed plateau of strength or softening at the level of several nanometers has not been detected in this study.

To further examine the strengthening and flow behavior of the various samples, we have also performed microcompression experiments on pillars machined from the Mg/Ti multilayers using FIB. Fig. 2 displays a representative image of such a micropillar. It shows that the average diameter of this pillar is  $\sim 0.5 \mu\text{m}$  in an attempt to maintain a height/diameter aspect ratio of 2:1 [54]. For pillars of

such dimensions, tapering becomes an unavoidable issue [65,66], which may introduce spurious strain hardening according to the work of Zhang et al. [54]. To measure the stress, we use the cross-sectional area at half height of the multilayer pillar. Since machine compliance cannot be removed for such non-standard measurement and the strain is based on the apparent displacement of the flat punch recorded by the nanoindentation system, we have not attempted to derive the elastic modulus of the samples. Fig. 6 presents the representative true stress–strain plots of some Mg/Ti multilayers with different  $h$  values (2.5, 5.0 and 100 nm, respectively). We can see that the compressive strength of the multilayers has the same trend as the hardness values. However, in all the cases, the compressive strength is much higher than the “flow strength” derived from the nanoindentation experiments based on the Tabor relationship [51] ( $\sigma = H/C$ ,  $C$  being the constraint factor, taken to be 2.7 in this work). For example, Fig. 6 shows that the strength of the multilayer specimen with  $h = 2.5$  nm is  $\sim 2.4$  GPa, while the Tabor formula only leads to a flow strength in the amount of  $\sim 1.56$  GPa from nanoindentation. This apparent discrepancy will be discussed and explained in a later section.

It is also noticed from the microcompression results that the pillars start to soften after yielding. The scarcity in data points in the post-yielding phase is due to the limited data acquisition rate (only 20 Hz) of the Nanoindenter XP I used to perform the microcompression experiments. We will discuss the apparent flow softening in the next section of the paper.

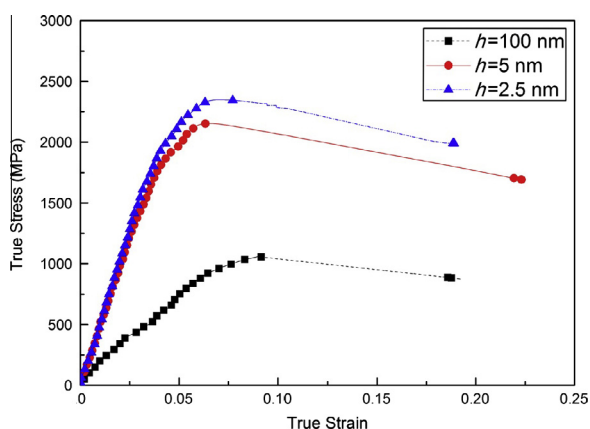


Fig. 6. True stress–strain curves from microcompression experiments of the Mg/Ti multilayer specimens with individual thicknesses of 2.5 nm, 5 nm and 100 nm, respectively. Because of the machine compliance, we do not attempt to derive the elastic modulus of the films. It is striking to notice that under microcompression, the multilayer specimens are much stronger than under nanoindentation. For example, when  $h = 2.5$  nm, the compressive strength is  $\sim 2.4$  GPa, much higher than the strength of  $\sim 1.56$  GPa derived based on nanoindentation. However, at large  $h$ , the discrepancy between compressive strength and the nanoindentation strength becomes less significant. It is also noticed that the specimen with  $h = 2.5$  nm has a strength level very close to the ideal strength of Ti/Mg, assuming the shear modulus of the multilayer specimen follows the rule of mixture. See the text for detailed explanation for this phenomenon.

Fig. 7a and b displays the pre-loading and post-loading images of the Mg/Ti multilayers with  $h \sim 100$  nm. Since the top layer is always Ti, we can infer that the layer with brighter contrast is Mg. The post-loading image (Fig. 7b) suggests that under compression, plastic deformation proceeds from the pillar top. Unlike observations where shear bands appear during microcompression of some multilayer samples [67–69], we have not seen shear bands in our specimens. But it can be observed that upon compression, the Mg phase has been squeezed out, or “extruded” out between the Ti layers (Fig. 7b). Fig. 8 gives an example of pre-loading (a) and post-loading (b) images of the Mg/Ti multilayer where  $h = 5$  nm. Due to the extremely small  $h$ , the individual layers cannot be distinguished from the image. However, the boundary between the multilayer and the silicon substrate can still be observed, as indicated by the arrows in Fig. 8a and b. Fig. 9 provides the pre-loading (a) and post-loading (b) images of the specimen with  $h = 2.5$  nm. In these specimens, no shear bands have been observed either. Plasticity proceeds from the pillar top. It is also suggested that the squeezing of the thicker Mg layers is attributed to the smaller interface area and weaker constraints from adjacent Ti layers. For the same reason, the deformation of extremely thin layers will be comparatively more difficult, resulting in a higher strength of the film.

Finally, we present the SRS results of the Mg/Ti multilayers based on nanoindentation at different loading rates, and the SRS of each specimen was calculated using Eq. (2), while the activation volume was derived from Eq. (3). Fig. 10 shows the  $\ln H$  vs.  $\ln \dot{\epsilon}$  plots of the various Mg/Ti multilayers. We can see that all the data points fall onto the respective straight lines. The slope of each straight line is the SRS of the corresponding specimen. The measured values of SRS ( $m$ ) and activation volume ( $V^*$ ) of the various specimens are listed in Table 2. The values of  $m$  for the Mg/Ti multilayers fall in the range of 0.038–0.053 and the activation volumes are in the range of  $3.7$ – $8.0b^3$  ( $b$  is the magnitude of the Burgers vector of dislocations). However, according to the results, it is quite difficult to come to a straightforward and clear relation between  $m$ ,  $V^*$  and individual layer thickness  $h$ , as that reported for Cu/Cr and Cu/Zr multilayers by Niu et al. [29]. Neither can a definitive relation between SRS,  $V^*$  and  $h$  be established for these Mg/Ti multilayer specimens in a way similar to the relationship between SRS and grain size  $d$  for bulk fcc and bcc metals [49]. If we compare the SRS values of the Mg/Ti multilayers with those of the monolithic constituents as shown in Table 3 (data points for Mg and Ti in various conditions are from Dorn and Mitchell [70], Trojanova et al. [71], Hwang et al. [72], Conrad [73] and Jia et al. [74]), no clear correlation can be identified either. We can see that the strength of Mg/Ti multilayers is not as sensitive to strain rate as nanocrystalline Mg, even when the layer thickness  $h$  is approaching to the grain size  $d$  ( $m = 0.0524$  at  $h = 50$  nm of this work vs.  $m = 0.45$  at  $d = 45$  nm from Refs. [71,72]). Unlike the remarkable change of SRS with grain size in pure monolithic Mg, the

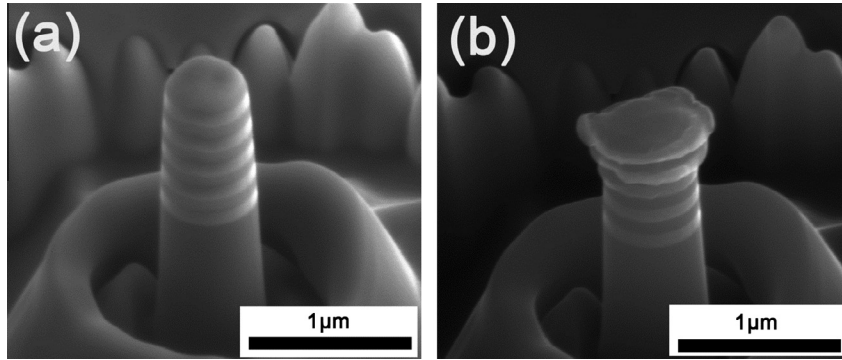


Fig. 7. Pre-loading (a) and post-loading (b) scanning electron micrographs of micropillars of the Mg/Ti multilayer specimen with  $h = 100$  nm. Since the top layer is always Ti, the layers of bright contrast are the Mg phase. The post-loading image indicates that under uniaxial compression, plastic deformation proceeds from the top of the pillar. It is also noticed that under compression, the Mg layers have been squeezed or extruded out between the mechanically more rigid Ti layers. No shear banding events can be observed.

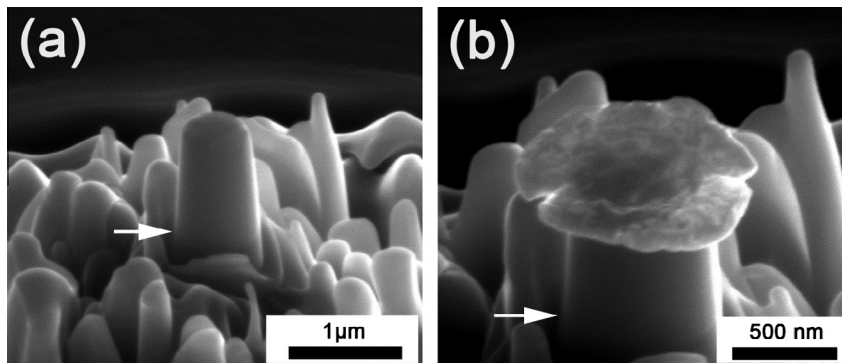


Fig. 8. Pre-loading (a) and post-loading (b) SEM images of micropillars of the Mg/Ti multilayer specimen with  $h = 5$  nm. In this case, even though the individual layers cannot be distinguished, the boundary between the multilayers and the silicon substrate is visible (see the arrows in both (a) and (b)). Again, under compression the plastic deformation proceeds from the top of the multilayer specimen, and no shear band can be observed.

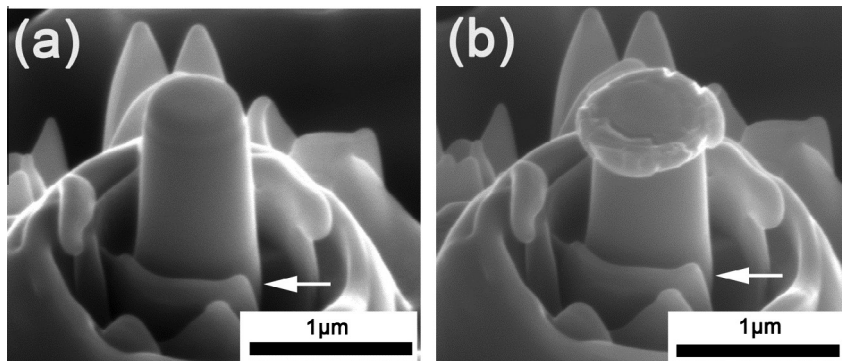


Fig. 9. Pre-loading (a) and post-loading (b) SEM images of micropillars of the Mg/Ti multilayer specimen with  $h = 2.5$  nm. Similar to other compression specimens, again, the plastic deformation proceeds from the top of the multilayer specimen, and no shear band can be observed.

Mg/Ti multilayers of this work do not show significant change in SRS when  $h$  is changed. This is also true for the activation volumes as suggested by the data in Table 2.

In summary, we have observed that the hardness of the Mg/Ti multilayer specimens follows the conventional Hall–Petch relation for relatively large  $h$ . The Hall–Petch strengthening levels off at smaller  $h$ . A dip in the hardness– $h^{-0.5}$  curve is observed at  $h = 5$  nm. However, with

further decrease in  $h$ , the hardness starts to increase again, and the highest hardness is obtained at the smallest  $h$  (2.5 nm) of this work. Microcompression experiments of these samples result in much higher strength vis-à-vis hardness measurement via the Tabor formula. Strain softening is observed after yielding under microcompression. No certain trend has been established for the SRS but the activation volume is smaller than  $10b^3$  for all the specimens.

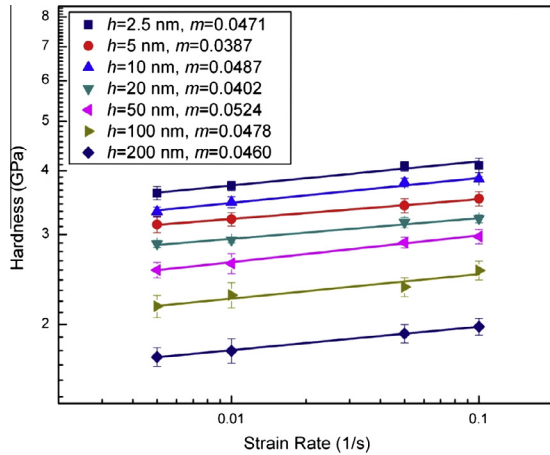


Fig. 10. Experimental results of SRS of the Mg/Ti multilayered specimens with different individual layer thicknesses. The results are based on instrumented nanoindentation at different loading rates. The results are plotted in double logarithmic scales. It shows that the  $\ln H$  and  $\ln \dot{\epsilon}$  can be well depicted by straight lines and the slopes of the straight lines are the SRS values of each specimen. The values of  $h$  and SRS ( $m$ ) are also provided in the inset of this plot.

#### 4. Discussion

In this part, we will try to provide an explanation for the microstructure and the mechanical behavior of the Mg/Ti multilayers. We will first discuss the microstructural evolution as a function of the individual layer thickness  $h$ , followed by the different potential strengthening mechanisms within the various thickness regimes. Finally, we will attempt to explain the much higher compressive strength with respect to the nanoindentation measurement results.

##### 4.1. Microstructure of the Mg/Ti multilayers

In addition to the significant difference in melting points between Mg and Ti ( $T_{m-Mg} = 923$  K vs.  $T_{m-Ti} = 1943$  K), these two metals have very limited solubility ( $\sim 2$  at.%) to

each other. The enthalpy of mixing between Mg and Ti is positive, and that is why there are no intermetallic compounds between Ti and Mg from their binary phase diagram [75]. This also means that at equilibrium, the inter-diffusivity between Ti and Mg is vanishingly small [76]. Therefore, it should be difficult to combine them together to form an alloy by regular preparing techniques. Asano et al. [77] reported the synthesis of  $Mg_xTi_{100-x}$  alloys by milling Mg and Ti powders for 50–200 h. They found that a high content of metastable phases with bcc or fcc structure had been introduced into these far-from-equilibrium alloys. Although in the work of Asano the crystallite size of the ball-milled  $Mg_xTi_{100-x}$  non-equilibrium alloys had been reduced to  $\sim 10$  nm, further reduction in grain size with uniform grain size distribution had been proved to be impossible. In contrast, the deposition of Mg and Ti by magnetron sputtering reported in the present work offers an effective way to produce Mg–Ti composites with high thermal stabilities as well as accurate controls of specimen size. The very limited inter-mixing between Ti and Mg adds one more advantage in that we should expect clean Mg/Ti interfaces, which simplifies the problem and allows us to explore the dislocation mechanisms responsible for the strengthening effects as a function of  $h$ . The thermal and structural stability of Mg and Ti in the multilayers renders this binary system a very good model system for the study of the microstructure and mechanical properties of hcp/hcp multilayers.

Based on our XRD and TEM results, there are three features worth noting about the microstructure of Mg/Ti multilayers. First, no phase transformation or change of lattice structure has been detected. For nanostructured multilayers made up of metallic constituents with different atomic configurations at the interface, one component is prone to transform into the crystal structure of another to accommodate the significant lattice mismatch. This phenomenon has been widely observed [12], especially when an hcp metal is involved. For instance, a metastable

Table 2  
SRS  $m$  and activation volume  $V^*$  of Mg/Ti multilayers with  $h$ .

$h$ (nm)	2.5	5	10	20	50	100	200
$m$	0.0471	0.0387	0.0487	0.0402	0.0524	0.0478	0.0460
$V^*$	$3.713b^3$	$5.280b^3$	$3.860b^3$	$5.515b^3$	$4.688b^3$	$6.063b^3$	$7.978b^3$

Note: the parameter  $b$  here indicates the average length of Burgers vector of Mg and Ti.

Table 3  
The comparison of  $m$  in Mg/Ti multilayers with Mg and Ti in different conditions.

Material	$m$	Ref.
Single crystal Mg (Dorn and Mitchell)	0.041	[70]
Nanocrystalline Mg, $d \sim 100$ nm (Trojanova)	0.31	[71]
Nanocrystalline Mg, $d \sim 45$ nm (Hwang et al.)	0.6	[72]
Polycrystalline Ti, $d \sim 0.05$ mm (Conrad)	0.025	[73]
Ultrafine grained Ti, $d \sim 260$ nm (Jia et al.)	0.009	[74]
Mg/Ti multilayered nanofilms	0.038–0.053	This work

Note:  $d$  is the average grain size.

bcc Mg phase was reported by Ham and Zhang in the sputter-deposited Mg/Nb multilayers with  $h$  of 5 nm or less [38]. Similarly, Zr has also been found to have an hcp-to-bcc transition during room-temperature deposition of Nb/Zr multilayers, as described in the work of Lowe and Geballe [78]. The Mg/Ti multilayer system in this study, however, keeps the hcp crystal structure at various values of  $h$ . This may be attributed to the identical lattice type of Ti and Mg at room temperature.

Second, in contrast to most reported metallic multilayer systems, there is more than one orientation relationship identified between Ti and Mg in Mg/Ti multilayers when  $h > 2.5$  nm. According to the literature, fcc/bcc multilayered thin films generally follow the Kurdjumov–Sachs (K–S) orientation relationship [27,34], in addition to occasional observation of the Nishiyama–Wasserman (N–W) relationship [79]. The fcc/fcc multilayers are featured by cube-on-cube crystallographic relationship with (111) fiber texture, of which Cu/Ag, Ag/Ni and Cu/330 stainless steel multilayers are examples [14,35,80]. Considering that Mg and Ti are both hcp metals with a moderate lattice parameter mismatch between them, the hcp-on-hcp orientation (OR.1) should be favored. The prevalence of (0002) texture and OR.1 in the Mg/Ti multilayers is thus understandable. Zheng et al. have also observed a similar orientation relationship in vapor-quenched Ti–29 wt.% Mg alloy [81]. As for the emergence of OR.2 in the Mg/Ti multilayers with relatively large  $h$ , further effort may be needed to clarify the underlying mechanism, including modeling and simulations. For now we may invoke the work of Wei and Misra [82], who observed layer curvature manifested as the wavy morphology of the layers. Such curved layers may disrupt the orientation relationship at small  $h$ , and result in some other relationship such as OR.2 identified here with relatively large  $h$ . However, the formation of layer curvature is a complicated dynamic process influenced by thermal equilibrium during deposition, growth defects, surface diffusion and so on. It is therefore difficult to accurately predict the growth mechanisms of the Mg/Ti multilayers.

Third, the moderate lattice mismatch between hcp Ti and Mg indicates that the interface of the Mg/Ti multilayers should be semi-coherent at best. At the Ti/Mg interface, disregistry of atoms can be periodically taken up by misfit dislocations. It is well known that the interface characteristics play a vital role in the deformation mechanisms of multilayered materials. The effects of partially relieved coherency strain and misfit dislocations at the Mg/Ti interface on the mechanical behavior of Mg/Ti multilayers will be discussed in detail in the following section.

We should point out that the epitaxial growth between the Ti and the Mg layers needs further elaboration because of the relatively large lattice mismatch between the two hcp metals. The degree of epitaxy depends on a number of factors. As such a critical thickness can be derived for different systems. In the Mg/Ti system, we can use the following formula to estimate the critical thickness  $h_{cr}$  of epitaxial growth [83–85]:

$$h_{cr} = \frac{b}{2\pi\varepsilon_m} \ln \left( \frac{\sqrt{2}h_{cr}}{b} \right) \quad (4)$$

where  $b$  is the length of Burgers vector and  $\varepsilon_m$  is the misfit strain of the film. The physical meaning of  $h_{cr}$  is that it gives the theoretical critical thickness for the formation of misfit dislocations to relax the misfit strains. When  $h_{cr}$  is too small, the energy from the constrained layers will not be enough to provide the energy required to form the misfit dislocations.

Here, we assume only dislocations with an  $a$ -type Burgers vector are operating, and  $\vec{b} = 1/3\langle 11\bar{2}0 \rangle$  while the misfit strain is 8.6%. According to Eq. (4), the stable critical thickness of Mg/Ti epitaxial growth is only 0.6 nm and comparable to several atomic monolayers. In other words, the appearance of misfit dislocations is inevitable in Mg/Ti multilayers to accommodate the lattice mismatch. The distance  $s$  between adjacent misfit dislocations is

$$s = \frac{b}{\varepsilon_m} \quad (5)$$

For Mg/Ti multilayers,  $s_{Mg-Ti}$  is  $\sim 3.55$  nm. It agrees with the HRTEM image of the Mg/Ti multilayer specimen with  $h = 2.5$  (Fig. 4c), where epitaxial growth can be clearly seen in the Mg/Ti interfacial region with a width of at least 3.0 nm.

As suggested by Matthews [86], in practice, the critical thickness  $h_{cr}$  for epitaxial growth could be larger than the value calculated by Eq. (4) since other strain relaxation factors, such as the elastic strain in the lattices or difficulties associated with the formation of misfit dislocations, are involved. Taking the shearing in the first two Ti atomic layers deposited right above Mg as an example, these stacking-fault-like distortions as shown in Fig. 4c could be responsible for relaxing strains in the films to a certain level and potentially extend the critical thickness for epitaxial growth.

When  $h$  is large, other orientation relationships such as OR.2 start to evolve. Based on this relationship, it is realized that the Ti crystals orient themselves with the dominant slip plane Ti  $\{01\bar{1}0\}$  paralleling to Mg  $\{0002\}$  which is the dominant slip plane of Mg at the interface, as  $h$  is increased. By reducing the angle between the dislocation glide plane and the interface, this kind of arrangement is favored for the dislocations to propagate across the interface and consequently weakens the strengthening effects from the interface barriers. It is energetically favorable for OR.2 to emerge when  $h$  is thick enough, while a smaller  $h$  might restrict this transformation and keep the epitaxial growth. It is at least a possible explanation for the appearance of OR.2. However, other potential fundamental mechanisms for its presence need further elaboration. For example, the entropic factor or strain energy reduction at large  $h$  may be carefully examined to show the effect, or the lack thereof.

## 4.2. Strengthening mechanisms in different regimes of $h$

In this part, we first provide a discussion on the nanoindentation behavior pertaining to the strengthening mechanisms of the Mg/Ti multilayers and their extraordinarily high hardness. Then we will discuss the discrepancy between the nanoindentation results and the microcompression results.

### 4.2.1. Strengthening effects responsible for hardness

First of all, we notice that the Mg/Ti multilayers exhibit much higher strength than the bulk counterpart of their constituents. For example, the ultimate tensile strength of pure Ti is  $\sim 550$  MPa [87], about one third of the maximum strength obtained from our Mg/Ti multilayers. Even cryomilled commercial-purity titanium with a high content of impurity atoms has a yield strength only at the level of  $\sim 900$  MPa [88]. As a matter of fact, the strength of the Mg/Ti multilayers with fine lamellar structure is so impressive that it even surpasses the strong commercial Ti–6Al–4V alloy (yield strength  $\sim 880$  MPa). This is even more so if we look at the microcompression results. The yield and ultimate tensile strengths of pure Mg in the sand-cast condition are only  $\sim 21$  MPa and  $\sim 90$  MPa, respectively [39]. Considering these factors, we believe it is necessary to provide an in-depth discussion about the extraordinarily high strength of the Mg/Ti multilayers.

We believe that the semi-coherent interface between the two hcp metals is partly responsible for the high strength of the Mg/Ti multilayers, especially when we make comparison with the mechanical properties of sputter-deposited Mg/Nb multilayers reported by Ham and Zhang [38] (the Mg/Nb results are also plotted in Fig. 5 for comparison). The measured peak hardness of the Mg/Nb system is only  $\sim 2.8$  GPa, which is also achieved at  $h = 2.5$  nm, much lower than  $\sim 4.2$  GPa of the Mg/Ti multilayer specimen with the same  $h$ . Meanwhile, the measured Hall–Petch slope of the Mg/Nb system is slightly smaller than that of the Mg/Ti system. Since the Hall–Petch slope represents the strength of interface barrier related to slip transmission, the peak strength of multilayers can be estimated from the measured slope by the following equation [23]:

$$\tau^* = \frac{k^2 \pi (1 - \nu)}{\mu b} \quad (6)$$

where  $\tau^*$  is the barrier strength of the boundary for slip transmission,  $\nu$  is the Poisson ratio,  $\mu$  the shear modulus and  $b$  is the length of the Burger vector. The value of the parameter  $k$  in Eq. (6) under shear loading is obtained by dividing  $k_\sigma$  with a Taylor factor of  $\sim 3.1$ . Similar to Mg/Nb, the substitution of relevant parameters of Mg into Eq. (6) will lead to an overestimation of the strength of the Mg/Ti multilayers. Here, we used  $\nu = 0.32$ ,  $\mu = 44$  GPa and  $b = 0.29$  nm, all of which are from the stiffer component, Ti, into the equation and obtained  $\tau^* = 0.44$  GPa. By multiplying  $\tau^*$  with the Taylor factor, we can obtain a theoretical estimate of the ultimate peak

strength of the Mg/Ti multilayers,  $\sim 1.36$  GPa, not very far away from the experimental peak strength of  $\sim 1.56$  GPa (see Fig. 5).

The above estimation of interface boundary strength (IBS) is mainly based on dislocations pile-up against the interface. We can also attempt to predict the peak strength alternatively by considering the intrinsic properties of the Mg/Ti interface. First, we calculate the image stress in the Mg/Ti multilayers owing to the elasticity mismatch between Mg and  $\alpha$ -Ti. As we know, the dislocation which is moving from the soft layer to a hard layer must overcome a repulsive force (so-called image stress or Koehler stress) due to the different shear moduli across the interface. The upper bound of the image stress in the Mg/Ti multilayer can be calculated as [5]

$$\tau_{image} = \frac{\mu_{Ti} - \mu_{Mg}}{\mu_{Ti} + \mu_{Mg}} \frac{\mu_{Mg} \sin \theta}{8\pi} \quad (7)$$

where  $\theta$  is the smallest angle between the interface and the glide planes of the crystal and is assumed to be  $60^\circ$  for Mg/Ti multilayers. We can then calculate the image stress to be  $\tau_{image} \sim 0.26$  GPa. In addition, the arrays of misfit dislocations deposited on this semi-coherent interface can also impede the slip transmission of dislocations, which is [21,89]

$$\tau_{misfit} = \alpha \mu \left( \xi - \frac{b}{2h} \right) \quad (8)$$

where  $\alpha$  is the Saada's constant and is  $\sim 0.5$ ;  $\xi$  is the misfit strain (8.6%). At  $h = 2.5$  nm,  $\tau_{misfit}$  is calculated to be 0.19 GPa.

The applied stress required for the glide of dislocations across the interface is mainly from these two parts, and therefore

$$\sigma_{IBS} \approx M(\tau_{image} + \tau_{misfit}) \quad (9)$$

The theoretical peak strength for the Mg/Ti multilayers is therefore  $\sim 1.40$  GPa, in reasonable agreement with the experimental result of  $\sim 1.56$  GPa. The small discrepancy may be attributed to the coherency stress of the Mg/Ti interface, since the interface might not be completely relaxed. Based on atomistic simulations on Cu/Ni epitaxial nanolayers, Rao and Hazzledine claimed that the coherency stress is capable of enhancing the Koehler barrier by changing the elastic constants of the constituent components and the dislocation core width [89].

We have seen that the Hall–Petch law does give a good fitting to the strength of the Mg/Ti multilayers when  $h > 50$  nm. However, it significantly overestimates the flow strength as  $h$  is less than 20 nm. The failure of the Hall–Petch law in this regime is probably because of the incapability of dislocation pile-up against the interface. For example, in the case of the double-ended pile-up, there should be at least three dislocations to make the pile-up model valid. However, when  $h$  is below 50 nm, the number of dislocations that can survive the tiny space can be vanishing. As a consequence, the plastic deformation of Mg/Ti multilayers at this length scale is mainly mediated by the

glide of dislocation loops confined within softer layers. As such, the Orowan bowing mechanism is suggested to describe the behavior by  $\sigma \propto \ln(h'/b)/h'$  [21,90–92], where  $h'$  is the layer thickness measured parallel to the glide plane and is taken as  $2h/\sqrt{3}$ , assuming pyramidal slip in hcp structure under indentation. This confined layer slip (CLS) model fits the experimental data well at the vicinity of  $h = 20$  nm. But it greatly overestimates the flow strength for  $h \leq 10$  nm.

Here, we follow a refined CLS model by Misra et al. [23] to better interpret the trend of flow strength of the Mg/Ti multilayers for  $h$  from 2.5 to 20 nm. The stress required to activate this mechanism is given by:

$$\sigma_{\text{CLS}} = M \frac{\mu_b}{8\pi h'} \left( \frac{4-\nu}{1-\nu} \right) \left[ \ln \frac{\alpha h'}{b} \right] + \frac{\mu b}{\lambda(1-\nu)} - \frac{f}{h} \quad (10)$$

The first term in Eq. (10) represents the normal stress needed to propagate the glide loop trapped between adjacent interfaces. It is directly derived from the original CLS model but includes possible change in dislocation core width. Due to the prevalent hcp-on-hcp orientation in the Mg/Ti multilayers and basal slip as the dominant slip mode in Mg with its basal plane parallel to the interface, the absorption of glide dislocation will occur at the interface. Instead of a compact core ( $\alpha = 1$ ), an expanded dislocation core is therefore preferred in the case of the Mg/Ti interface. The second term in Eq. (10) is the blocking strength from the interaction of a single glide dislocation with the dislocations that reside on the interface. In Misra's work, the dislocation segments on the interface are deposited by previous glide loops. Nevertheless, these glide loops could not only create dislocations on the interface but also annihilate the misfit dislocations that has already been formed by the lattice mismatch. As a result, the spacing of the in-plane dislocation segments might be larger than that of

misfit dislocations without rearrangements. The last term corresponds to the elastic interface stress which will facilitate the yielding of multilayers under compression, while  $f$  is usually in the range of 2–3 J m<sup>-2</sup>. With all the considerations mentioned above, we use  $\alpha = 0.6$ ,  $f = 3$  J m<sup>-2</sup> and  $\lambda = 9$  nm. The strength based on the refined CLS model is calculated and presented in Fig. 11 for small  $h$ . We see that the refined CLS model provides a good estimate for  $2.5 \leq h \leq 20$  nm.

Now a few final words about the physical significance of the SRS and activation volumes of the Mg/Ti multilayer specimens. Though not much can be inferred from the experimental results (Fig. 10 and Table 2) regarding the definitive effect of  $h$  on those two parameters, the order of magnitude of the activation volumes suggests that some local dislocation activities with small sampling volume ( $\sim 7b^3$ ) are responsible for the plastic deformation of the films. This is consistent with the above discussion. It is also seen from Table 2 that, particularly when  $h$  is relatively large, there is a trend that the activation volume generally increases with  $h$ . This is understandable as when  $h$  is large, the sampling length of the dislocation activities should be large accordingly.

#### 4.2.2. Discrepancy between nanoindentation hardness and microcompression strength

As we have noticed, the microcompression strength is much higher than the strength measured by nanoindentation. The compression strength of the Mg/Ti multilayer with the smallest  $h$  is  $\sim 2.4$  GPa. It should be a reasonable assumption that the shear moduli of the multilayer specimens also follow the rule of mixture. This leads to a shear modulus of these multilayers in the amount of  $\sim 30$  GPa. In other words, the  $h = 2.5$  nm multilayer has nearly reached the theoretical or ideal strength of the constituent components combined. This has also been reported in other multilayer systems [85]. When  $h$  is larger, this discrepancy becomes less significant. To reconcile the apparent discrepancy as well as its trend, we need first to examine the plastic deformation mechanisms of single-crystal titanium and magnesium.

First, the dominant slip system of single-crystal  $\alpha$ -Ti is the prismatic slip at relatively low temperatures such as room temperature and below [93–96]. The prismatic slip systems are  $\langle 11\bar{2}0 \rangle \{10\bar{1}0\}$ , with a Burgers vector of  $1/3\langle 11\bar{2}0 \rangle$ . Other secondary slip systems have also been identified such as the basal slip ( $\langle 11\bar{2}0 \rangle \{0001\}$ ) and pyramidal slip ( $\langle 11\bar{2}0 \rangle \{10\bar{1}1\}$ ), whose Burgers vectors are all  $1/3\langle 11\bar{2}0 \rangle$ . Dislocations with this type of Burgers vector are the so-called  $\langle a \rangle$ -type dislocations. Under certain conditions, especially in  $\alpha$ -Ti with impurities,  $\langle a + c \rangle$  type dislocations may operate, though the motion of these requires a much higher stress level. In addition to these slip modes,  $\alpha$ -Ti also exhibits six twinning modes, three of which operate under compression along the  $c$ -axis and three under tension along the  $c$ -axis. The twinning planes for the compression modes are  $\{11\bar{2}4\}$ ,  $\{11\bar{2}2\}$ ,  $\{10\bar{1}1\}$ ; those for tension modes are  $\{11\bar{2}3\}$ ,  $\{11\bar{2}1\}$ ,  $\{10\bar{1}2\}$  [97].

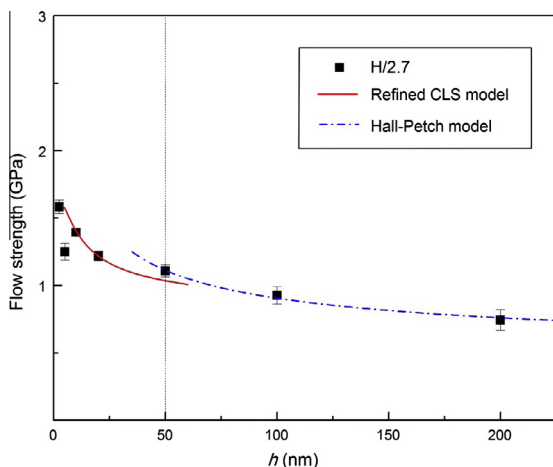


Fig. 11. The fitting results of the indentation-based flow strength of the Mg/Ti multilayer specimens based on the Hall–Petch relation ( $h \geq 50$  nm) and the modified confined layer slip (CLS) model ( $h < 50$  nm). It shows that the modified CLS model provides a very good prediction of the indentation-based flow strength of the Mg/Ti multilayer specimens at smaller  $h$ .

As for pure single-crystal magnesium, the predominant slip system is the basal slip. It has been found that the critical resolved shear stress (CRSS) for basal, prismatic and pyramidal slips are  $\leq 1.0$ ,  $\sim 50$  and  $\sim 44$  MPa, respectively [98] (and references therein). It has also been reported that the CRSS for twinning in single-crystal Mg when loaded along the *c*-axis is  $\sim 90$  MPa [99]. Therefore, unlike most cubic metals where the predominant slip systems have nearly the same level of CRSS values, the slip systems of hcp metals can be classified into “hard” ones and “soft” ones, and which one will operate depends on the crystal orientation and the relative ease of the individual slip systems [100].

Our TEM and XRD characterizations have confirmed that when *h* is very small, we have only observed epitaxial growth between Mg and Ti, with Mg  $\{0002\}$ //Ti  $\{0002\}$ . What is more, the *c*-axis of both the Ti and the Mg layers are normal to the surface of the film. Under uniaxial compression perpendicular to the specimen surface, this orientation relationship translates to a vanishing Schmid factor for the entire dominant and “easy” slip systems, for both Ti and Mg. In other words, under uniaxial compression, both the Mg and Ti crystals in the multilayer specimen with small *h* have a “hard” orientation. Now we can see that for the Mg/Ti multilayer specimens, compression should result in a high strength simply due to “geometric” hardening.

Under nanoindentation, the stress state within the specimen is much more complicated. But naturally, one should expect shear and tensile stress components within the layers [101], which result in non-vanishing resolved shear stress on those dominant and easy slip systems. This results in the multilayer films behaving as if they were “softer” under nanoindentation condition than under uniaxial compression along the *c*-axis of Ti and Mg.

When *h* is increased beyond a point, other orientation relationships, such as OR.2 (Mg  $\{0002\}$ //Ti  $\{01\bar{1}0\}$  and Mg  $\langle 11\bar{2}0 \rangle$ //Ti  $\langle 0001 \rangle$ ), start to emerge. In this case, some mechanically soft and easy orientations can exist within the multilayer specimens, such as the prismatic planes of Ti, rendering a decreased compressive strength. It should also reduce the discrepancy between the nanoindentation-derived strength and microcompression strength.

We should point out that this discrepancy between indentation strength and compression strength, particularly the underlying mechanism, only applies to hcp/hcp multilayer systems. In cubic/cubic multilayer systems, it has also been observed that the compressive strength is higher. Atomistic simulations suggest that this is because the interface is relatively weak under shear, which contributes to the impressive ductility of the yet extremely strong multilayer films, since it allows dislocations to be deposited at the interfaces. This is also used to explain the observation of shear bands under microcompression of certain cubic/cubic multilayer systems [68,69,102].

Finally, the apparent flow softening in the microcompression stress–strain curves may be understood by the

operation of relatively soft slip systems once the peak stress is achieved as the crystals within the multilayers may change their orientations. Further efforts, particularly atomistic simulations or crystal plasticity modeling, may be needed to validate this notion.

## 5. Summary and concluding remarks

In this work, we have presented the first comprehensive investigation on an hcp/hcp multilayer system. The Mg/Ti multilayers were deposited onto single-crystal silicon substrates using magnetron sputtering at room temperature with equal individual thickness of the Mg and Ti layers, but the individual thickness *h* ranges from 2.5 to 200 nm. Based on the experimental results and discussion, we have reached the following conclusions.

When *h* is small, both XRD and TEM suggest a single orientation relationship between Mg and Ti. This relationship is Mg  $\{0002\}$ //Ti  $\{0002\}$  and Mg  $\langle 01\bar{1}0 \rangle$ //Ti  $\langle 01\bar{1}0 \rangle$  (or Mg  $\langle 2\bar{1}\bar{1}0 \rangle$ //Ti  $\langle 2\bar{1}\bar{1}0 \rangle$  with in-plane rotation of crystals). HRTEM also indicates an epitaxial relationship between the Ti and Mg layers at small *h*. When *h* is large, another orientation relationship emerges, which is Mg  $\{0002\}$ //Ti  $\{01\bar{1}0\}$  and Mg  $\langle 2\bar{1}\bar{1}0 \rangle$ //Ti  $\langle 0001 \rangle$ .

Nanoindentation experiments on the Mg/Ti multilayers show that at relatively large *h*, the hardness follows the Hall–Petch relation. At relatively small *h*, the Hall–Petch slope levels off. But a plateau has not been reached. The maximum hardness is obtained at the smallest *h*. The trend of the indentation derived strength of the multilayers can be predicted quite well by the modified CLS model at small *h*. The peak strength agrees well with theoretical predictions based on interface barrier strength and image stress evaluations.

Microcompression experiments of the multilayers yield much higher strength than that derived based on nanoindentation. For example, microcompression strength of the specimen with the smallest *h* (2.5 nm) is nearly as high as the theoretical strength, assuming that the shear modulus of the multilayer follows the rule of mixture. The discrepancy between the indentation strength and the microcompression strength can be explained by the nearly vanishing Schmid factors of all the fundamental slip systems of both Ti and Mg layers under uniaxial compression. That is to say, particularly for the Mg/Ti multilayer specimens with small *h*, the Mg and Ti layers have the hard orientation with respect to the loading direction. Such discrepancy starts to tone down when *h* is increased because some geometrically soft orientations such as OR.2 start to operate. This observation should be unique for hcp/hcp systems due to their special lattice structures and unique plasticity modes. The flow softening after yielding under microcompression might be explained by the activation of relatively easy slip systems due to rotation of the crystals.

No shear bands have been observed in the microcompression experiments. It appears that under uniaxial

compression, plastic deformation proceeds from the top of the pillars. Squeezing out of the Mg layers between the relatively rigid Ti layers was observed.

While this is the first attempt to investigate the microstructure and mechanical properties of an hcp/hcp system, some very interesting experimental results have been obtained. It would be exciting to examine other hcp metals in the context of hcp/hcp multilayers, such as Zn, Be, and Zr, and so on.

## Acknowledgements

Y.Y.L. expresses her gratitude to the Education Ministry of the People's Republic of China for the financial support during her graduate study at the University of North Carolina at Charlotte. Q.W. has been supported by the US Army Research Laboratory under Contract No. W911QX-08-C-0073. S.N.Y. has been supported by National Science Foundation through ERC.

## References

- [1] Kelly A, McMillan NH. *Strong solids*. Oxford: Clarendon Press; 1985.
- [2] Veprek S. *J Vac Sci Technol A* 1999;17:2401.
- [3] Misra A, Kung H, Embury JD. *Scr Mater* 2004;50:707.
- [4] Was GS, Foecke T. *Thin Solid Films* 1996;286:1.
- [5] Koehler JS. *Phys Rev B* 1970;2:547.
- [6] Zhang H, Wang XL, Qiao YQ, Xia XH, Tu JP. *Appl Surf Sci* 2011;257:5759.
- [7] Wang YM, Li J, Hamza AV, Barbee TW. *PNAS* 2007;104:11155.
- [8] Bajt S, Alameda JB, Barbee TW, Clift WM, Folta JA, Kaufmann B, et al. *Opt Eng* 2002;41:1797.
- [9] Barbee Jr T. *Sci Technol Rev* 1997.
- [10] Ruggiero ST, Barbee Jr TW, Beasley MR. *Phys Rev B* 1982;26:4894.
- [11] Ouyang LZ, Wang H, Chung CY, Ahn JH, Zhu M. *J Alloys Compd* 2006;422:58.
- [12] Zhang JY, Zhang P, Zhang X, Wang RH, Liu G, Zhang GJ, et al. *Mater Sci Eng A Struct Mater Prop Microstruct Process* 2012;545:118.
- [13] Kang BC, Kim HY, Kwon OY, Hong SH. *Scr Mater* 2007;57:703.
- [14] McKeown J, Misra A, Kung H, Hoagland RG, Nastasi M. *Scr Mater* 2002;46:593.
- [15] Wang YC, Misra A, Hoagland RG. *Scr Mater* 2006;54:1593.
- [16] Bhattacharyya D, Mara NA, Dickerson P, Hoagland RG, Misra A. *J Mater Res* 2009;24:1291.
- [17] Lima AL, Zhang X, Misra A, Booth CH, Bauer ED, Hundley MF. *Thin Solid Films* 2007;515:3574.
- [18] Li N, Wang J, Misra A, Huang JY. *Microsc Microanal* 2012;18:1155.
- [19] Anderson PM, Bingert JF, Misra A, Hirth JP. *Acta Mater* 2003;51:6059.
- [20] Zhang JY, Zhang X, Wang RH, Lei SY, Zhang P, Niu JJ, et al. *Acta Mater* 2011;59:7368.
- [21] Liu Y, Bufford D, Wang H, Sun C, Zhang X. *Acta Mater* 2011;59:1924.
- [22] Fu EG, Li N, Misra A, Hoagland RG, Wang H, Zhang X. *Mater Sci Eng A Struct Mater Prop Microstruct Process* 2008;493:283.
- [23] Misra A, Hirth JP, Hoagland RG. *Acta Mater* 2005;53:4817.
- [24] Misra A, Hirth JP, Kung H. *Philos Mag A Phys Condens Matter Struct Defect Mech Prop* 2002;82:2935.
- [25] Misra A, Demkowicz MJ, Wang J, Hoagland RG. *JOM* 2008;60:39.
- [26] Hoagland RG, Mitchell TE, Hirth JP, Kung H. *Philos Mag A Phys Condens Matter Struct Defect Mech Prop* 2002;82:643.
- [27] Misra A, Verdier M, Lu YC, Kung H, Mitchell TE, Nastasi N, et al. *Scr Mater* 1998;39:555.
- [28] Anderson PM, Li C. *Nanostruct Mater* 1995;5:349.
- [29] Niu JJ, Zhang JY, Liu G, Zhang P, Lei SY, Zhang GJ, et al. *Acta Mater* 2012;60:3677.
- [30] Hoagland RG, Kurtz RJ, Henager CH. *Scr Mater* 2004;50:775.
- [31] Ramaswamy V, Nix WD, Clemens BM. *Scr Mater* 2004;50:711.
- [32] Carpenter JS, Misra A, Uchic MD, Anderson PM. *Appl Phys Lett* 2012;101.
- [33] Carpenter JS, Vogel SC, LeDonne JE, Hammon DL, Beyerlein IJ, Mara NA. *Acta Mater* 2012;60:1576.
- [34] Kim Y, Budiman AS, Baldwin JK, Mara NA, Misra A, Han SM. *J Mater Res* 2012;27:592.
- [35] Zhang X, Misra A, Wang H, Shen TD, Nastasi M, Mitchell TE, et al. *Acta Mater* 2004;52:995.
- [36] Han WZ, Carpenter JS, Wang J, Beyerlein IJ, Mara NA. *Appl Phys Lett* 2012;100.
- [37] Zhang JY, Lei S, Liu Y, Niu JJ, Chen Y, Liu G, et al. *Acta Mater* 2012;60:1610.
- [38] Ham B, Zhang X. *Mater Sci Eng A Struct Mater Prop Microstruct Process* 2011;528:2028.
- [39] Avedesian MM, Baker H. *Magnesium and magnesium alloys*. Materials Park, OH: ASM International; 1999.
- [40] Koike J, Kobayashi T, Mukai T, Watanabe H, Suzuki M, Maruyama K, et al. *Acta Mater* 2003;51:2055.
- [41] Agnew SR, Duygulu O. *Int J Plast* 2005;21:1161.
- [42] Britton TB, Liang H, Dunne FPE, Wilkinson AJ. *Proc R Soc A* 2010;466:695.
- [43] Honeycombe RWK. *The plastic deformation of metals*. Baltimore, MD: American Society for Metals (ASM); 1984.
- [44] Baldi A, Pálsson GK, Gonzalez-Silveira M, Schreuders H, Slaman M, Rector JH, et al. *Phys Rev B* 2010;81:224203.
- [45] Beyerlein IJ, Mara NA, Wang J, Carpenter JS, Zheng SJ, Han WZ, et al. *JOM* 2013;64:1192.
- [46] Yashar PC, Sproul WD. *Vacuum* 1999;55:179.
- [47] Yang Q, Zhao LR. *J Vac Sci Technol A* 2003;21:558.
- [48] Buckle H. In: Westbrook JH, Conrad H, editors. *The science of hardness testing and its research applications*. Metals Park, OH: The American Society for Metals; 1972. p. 453.
- [49] Wei Q. *J Mater Sci* 2007;42:1709.
- [50] Wei Q, Cheng S, Ramesh KT, Ma E. *Mater Sci Eng A* 2004;381:71.
- [51] Tabor D. *Proc R Soc London A* 1948;192:247.
- [52] Uchic MD, Dimiduk DM, Florando JN, Nix WD. *Science* 2004;305:986.
- [53] Mara NA, Bhattacharyya D, Hirth JP, Dickerson P, Misra A. *Appl Phys Lett* 2010;97:021909.
- [54] Zhang H, Schuster BE, Wei Q, Ramesh KT. *Scr Mater* 2006;54:181.
- [55] Soderberg H, Oden M, Molina-Aldareguia JM, Hultman L. *J Appl Phys* 2005;97.
- [56] Shull AL, Spaepen F. *J Appl Phys* 1996;80:6243.
- [57] Williams DB, Carter CB. *Transmission electron microscopy*. Berlin: Springer; 1996.
- [58] Narayan J, Larson BC. *J Appl Phys* 2003;93:278.
- [59] Narayan J. *Acta Mater* 2013;61:2703.
- [60] Oliver WC, Pharr GM. *J Mater Res* 1992;7:1564.
- [61] Meyers MA, Mishra A, Benson DJ. *Prog Mater Sci* 2006;51:427.
- [62] Li JCM. *Trans Metall Soc AIME* 1963;227:239.
- [63] Ashby MF. *Philos Mag* 1970;21:399.
- [64] Louchet F, Weiss J, Richeon T. *Phys Rev Lett* 2006;97:075504.
- [65] Schuster BE, Wei Q, Hufnagel TC, Ramesh KT. *Acta Mater* 2008;56:5091.
- [66] Wu XL, Guo YZ, Wei Q, Wang WH. *Acta Mater* 2009;57:3562.
- [67] Mara NA, Bhattacharyya D, Dickerson P, Hoagland RG, Misra A. In: Zhao Y, Liao X, editors. *Ductility of bulk, nanostructured materials*, vol. 633–634. Durnten-Zurich, Switzerland: Materials Science Forum, Trans Tech Publications Ltd; 2010. p. 647.

- [68] Mara NA, Bhattacharyya D, Dickerson P, Hoagland RG, Misra A. *Appl Phys Lett* 2008;92.
- [69] Mara NA, Bhattacharyya D, Hirth JP, Dickerson P, Misra A. *Appl Phys Lett* 2010;97.
- [70] Dorn JE, Mitchell JB. In: Zackey VF, editor. *High-strength materials*. New York: Wiley; 1965. p. 510.
- [71] Trojanova Z, Lukac P, Szaraz Z. *Rev Adv Mater Sci* 2005;10:437.
- [72] Hwang S, Nishimura C, McCormick PG. *Scr Mater* 2001;44:1507.
- [73] Conrad H. *Prog Mater Sci* 1981;26:123.
- [74] Jia D, Wang YM, Ramesh KT, Ma E, Zhu YT, Valiev RZ. *Appl Phys Lett* 2001;79:611.
- [75] Massalski TB. *Binary alloy phase diagrams*. Materials Park, OH: ASM International; 1990.
- [76] Shewmon P. *Diffusion in solids*. New York: McGraw-Hill; 1989.
- [77] Asano K, Enoki H, Akiba E. *J Alloys Compd* 2009;480:558.
- [78] Lowe WP, Geballe TH. *Phys Rev B* 1984;29:4961.
- [79] Bain JA, Chyung LJ, Brennan S, Clemens BM. *Phys Rev B* 1991;44:1184.
- [80] Yu K, Liu Y, Rios S, Wang H, Zhang X. *Surf Coat Technol* 2013.
- [81] Zheng JG, Partridge PG, Steeds JW, Wilkes DMJ, WardClose CM. *J Mater Sci* 1997;32:3089.
- [82] Wei Q, Misra A. *Acta Mater* 2010;58:4871.
- [83] Freund LB, Suresh S. *Thin film materials – stress, defect formation and surface evolution*. New York: Cambridge University Press; 2003.
- [84] Matthews JW, Blakeslee AE. *J Cryst Growth* 1974;27:118.
- [85] Misra A, Verdier M, Kung H, Embury JD, Hirth JP. *Scr Mater* 1999;41:973.
- [86] Matthews J. *J Vac Sci Technol* 1975;12:126.
- [87] Niinomi M. *Mater Sci Eng A Struct Mater Prop Microstruct Process* 1998;243:231.
- [88] Yin WH, Xu F, Ertorer O, Pan Z, Zhang XY, Kecskes LJ, et al. *Acta Mater* 2013;61:3781.
- [89] Rao SI, Hazzledine PM. *Philos Mag A* 2000;80:2011.
- [90] Embury J, Hirth J. *Acta Metall Mater* 1994;42:2051.
- [91] Anderson P, Foecke T, Hazzledine P. *MRS Bull Mater Res Soc* 1999;24:27.
- [92] Phillips MA, Clemens BM, Nix WD. *Acta Mater* 2003;51:3157.
- [93] Yoo MH. *Metall Trans A Phys Metall Mater Sci* 1981;12:409.
- [94] Akhtar A, Teghtsoonian E. *Metall Trans A Phys Metall Mater Sci* 1975;6:2201.
- [95] Akhtar A. *Metall Trans* 1975;A6:1105.
- [96] Paton NE, Backofen WA. *Metall Trans* 1970;1:2839.
- [97] Tan XL, Gu HC, Zhang SF, Laird C. *Mater Sci Eng A Struct Mater Prop Microstruct Process* 1994;189:77.
- [98] Hutchinson WB, Barnett MR. *Scr Mater* 2010;63:737.
- [99] Yoshinaga H. *Trans Jpn Inst Met* 1963;4:1.
- [100] Shen JH, Li YL, Wei Q. *Mater Sci Eng A* 2013;582:270.
- [101] Larsson PL, Giannakopoulos AE, Soderlund E, Rowcliffe DJ, Vestergaard R. *Int J Solids Struct* 1996;33:221.
- [102] Wang J, Misra A. *Curr Opin Solid State Mater Sci* 2011;15:20.